Modulation of the Cellular Uptake of DNA Origami through Control over Mass and Shape

Maartje M. C. Bastings,[†,‡,§,#,∞] Frances M. Anastassacos,[†,‡,§,∞] Nandhini Ponnuswamy,[†,‡,§,∞] Franziska G. Leifer,[†,‡,§] Garry Cuneo,[§] Chenxiang Lin,[†,‡,§,∇] Donald E. Ingber,[§,∥] Ju Hee Ryu,[*,†,‡,§,⊥] and William M. Shih[*,†,‡,§]

†Department of Cancer Biology, Dana-Farber Cancer Institute, 450 Brookline Avenue, Boston, Massachusetts 02215, United States

‡Department of Biological Chemistry and Molecular Pharmacology, Harvard Medical School, Boston, Massachusetts 02115, United States

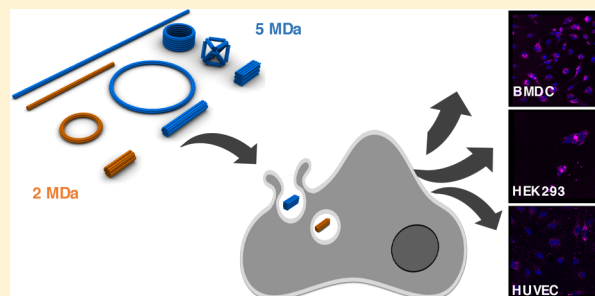§Wyss Institute for Biologically Inspired Engineering at Harvard, Boston, Massachusetts 02115, United States

∥School of Engineering and Applied Sciences, Harvard University, Cambridge, Massachusetts 02138, United States

⊥Center for Theragnosis, Biomedical Research Institute, Korea Institute of Science and Technology, Seoul 02792, Republic of Korea

S Supporting Information

ABSTRACT: Designer nanoparticles with controlled shapes and sizes are increasingly popular vehicles for therapeutic delivery due to their enhanced cell-delivery performance. However, our ability to fashion nanoparticles has offered only limited control over these parameters. Structural DNA nanotechnology has an unparalleled ability to self-assemble three-dimensional nanostructures with near-atomic resolution features, and thus, it offers an attractive platform for the systematic exploration of the parameter space relevant to nanoparticle uptake by living cells. In this study, we examined the cell uptake of a panel of 11 distinct DNA-origami shapes, with the largest dimension ranging from 50−400 nm, in 3 different cell lines. We found that larger particles with a greater compactness were preferentially internalized compared with elongated, high-aspect-ratio particles. Uptake kinetics were also found to be more cell-type-dependent than shape-dependent, with specialized endocytosing dendritic cells failing to saturate over 12 h of study. The knowledge gained in the current study furthers our understanding of how particle shape affects cellular uptake and heralds the development of DNA nanotechnologies toward the improvement of current state-of-the-art cell-delivery vehicles.

KEYWORDS: DNA origami, nanotechnology, cellular uptake, nanoparticles, structure−function relationship

In recent decades, nanoscale drug-delivery vehicles have been shown to favorably alter biodistribution and pharmacokinetics of conventional free therapeutis agents, often affording reduced renal clearance and improved targeting.[1,2] As such, a plethora of such nanoparticles (NPs) and formulation techniques have been developed. These aim to encapsulate naked drug molecules, including small-molecule, nucleic acid, and protein drugs, and appropriate them to specific tissues or cell-types. Specifically, these nanocarriers aim to overcome common hurdles experienced by free-floating drug agents such as enzymatic and chemical degradation, poor solubility, off-target effects and toxicity, and inability to bypass biological barriers (e.g., the cell membrane). Since 1990, multiple therapeutic NPs have undergone successful clinical trials and are now broadly applied in clinical settings. Despite these successes, a measurable deficiency exists in the over-arching purpose of drug delivery: to achieve maximal efficacy while minimizing off-target effects.

Consistent with the idea that the shape of pathogens contributes to their entry into host cells,[3] studies on cellular entry using synthetic nano- or microparticles have demonstrated a significant relation of particle size and shape to internalization efficiency in a cell-type-specific manner.[4,5] Shape and size thus have the potential to selectively increase uptake into a desired cell type while minimizing endocytosis by off-target cells. To date, multiple findings have demonstrated that material composition and size as well as surface charge influence the rate and overall uptake of nanoparticles.[6,7] An investigation of melanoma cell uptake of spherical polystyrene beads between 50−1000 nm in diameter revealed that the route of uptake differ depending on the particle size,[8] and 100 nm poly-lactic-co-glycolic acid (PLGA) nanoparticles were taken up 2- and 6-fold more efficiently by mass than 1 or 10 μm particles, respectively, in Caco-2 intestinal epithelial cells.[9]
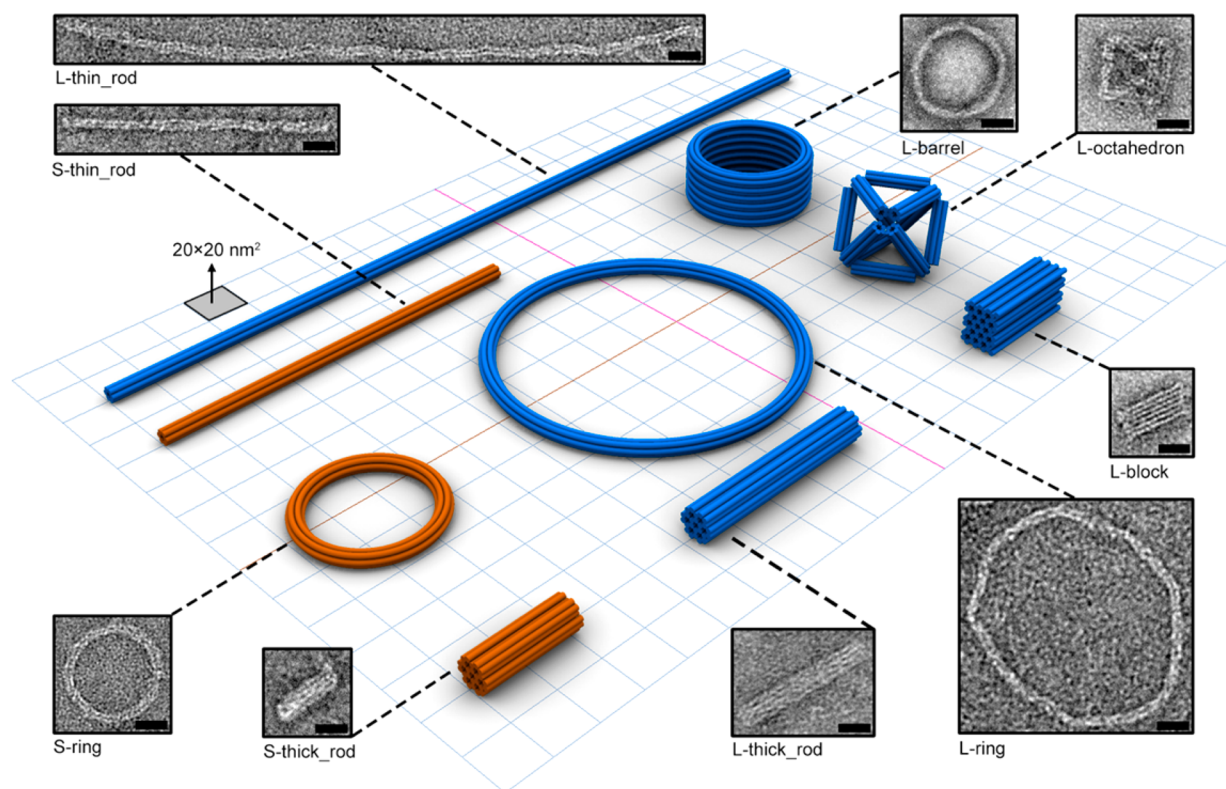
Figure 1. Computer models and TEM images of DNA origami nanoparticle designs. From left to right: top, L-thin_rod (7 nm × 400 nm); S-thin_rod (7 nm × 170 nm); L-barrel (60 nm outer diameter); L-octahedron (50 nm for largest dimension); L-block (16 nm × 21 nm × 50 nm) and bottom, S-ring (60 nm outer diameter); S-thick_rod (15 nm × 40 nm); L-thick_rod (15 nm × 100 nm); and L-ring (140 nm outer diameter). The scale bars are 20 nm. In the computer models, each cylinder represents one DNA double-helix. S structures are orange, and L structures are blue. Not pictured are the two (S and L) double-stranded scaffold controls (S-dsDNA and L-dsDNA).

Particle aspect ratio is also an important determinant of cellular uptake. The adhesive forces between the particle surface and cell membranes and the energy required for the membrane to deform around the particle can induce or prevent internalization in cells.[10,11] Studies using cationic cross-linked polyethylene glycol (PEG) nanoparticles have reported that increasing the nanoparticle (NP) aspect ratio promotes cellular uptake,[11] while the inverse has been observed with gold and polymer NPs.[10−13] Other studies report that mammalian epithelial and immune cells preferentially internalize disc-shaped NPs compared with nanorods and lower-aspect-ratio nanodiscs.[14] Lastly, the size and shape of NPs can also have a significant impact on biodistribution. For example, filamentous engineered NPs of sizes 2, 4, 8, and 18 μm were observed to have different half-lives, with the 8 μm NPs (the approximate diameter of blood cells) exhibiting the longest time in the circulation.[15]

Although these investigations are informative, it is difficult to compare their results because, in each case, the particles studied differed in composition and charge. The mass and volume of the particles also differ between studies, and the method of scoring internalization efficiency differed as well (e.g., the percentage of cells exhibiting particle uptake versus the number of particles taken up per cell). Furthermore, nanofabrication techniques used in these studies do not allow for the construction of a diverse range of shapes with nanoscale control. To go beyond these initial results and dissect in finer detail how NP shape, size, and surface functionalization influence cellular uptake, new fabrication methods with greater control over 3D form and shape are required.

Structural DNA nanotechnology[16,17] offers a precise method for the control of NP shape. The DNA-origami method, in particular, enables the controlled self-assembly of 2D and 3D custom-shaped nanostructures on the 10−100 nm scale with subnanometer precision features.[18,19] In this method, a long single-stranded M13 bacteriophage genome is folded via Watson−Crick base pairing of short single-stranded oligonucleotides to form multimegadalton (MDa) particles approximating any desired 3D form. Each staple strand bears a unique sequence and, therefore, a distinct spatial address within the nanostructure. Because DNA oligonucleotides can be synthesized with an extraordinary variety of chemical tags at each base position, DNA origami can be self-assembled with a large number of chemically distinct and site-specific functionalities.

These features render DNs a unique platform for drug delivery. As such, multiple studies have evaluated the propensity of DNs to deliver therapeutic molecules in a controlled and precise manner.[20] However, DNs required substantial concentrations of divalent cation (4−18 mM $MgCl_2$) to be present to retain their structural integrity. Multiple coating methods have been employed to prevent degradation in low-salt conditions and protection from nucleases in serum conditions; in particular, oligolysine has been found to do so without significant distortion of 3D structure.[21−23] To gain a better understanding of the influence of the size, shape, and aspect ratio on endocytosis, we studied the cellular uptake of a diverse library of DNA nanostructures (DNs) of uniform mass (2 and 5 MDa) and surface charge in mammalian cell lines relevant for therapeutic drug delivery. A
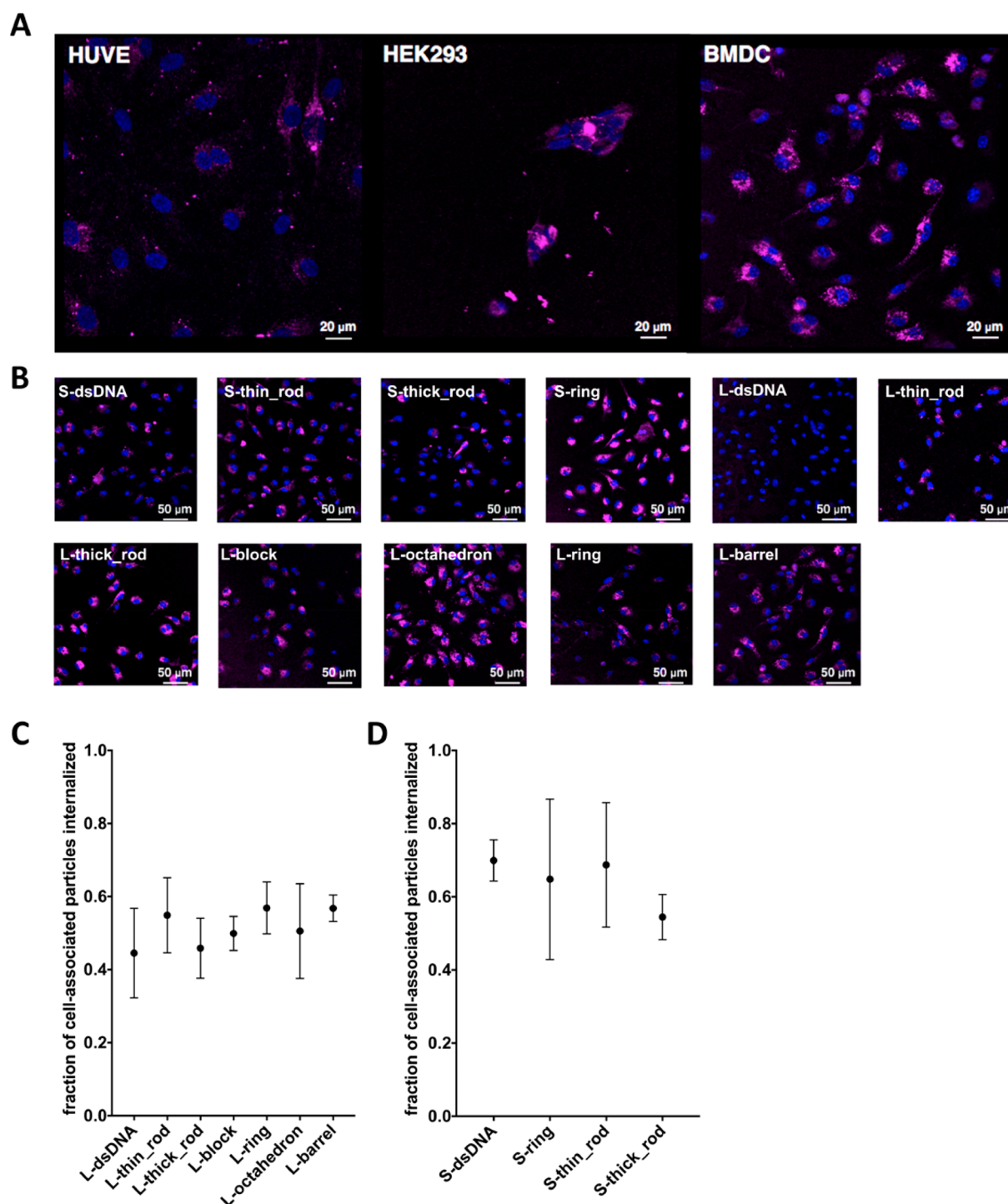
Figure 2. Analysis of shape internalization in three different cell lines. (A) 12 h incubation of 1 nM DN (L-barrel) with HUVE cells, HEK293 cells, and BMDCs. Nuclei can be seen in blue (Hoechst 33324), and DNs are represented in pink (Cy5-labeled DNA handles are present in each DN). The presence of DNs appears similar among all cell lines and does not affect viability. Full overview of all shapes in HUVE and HEK293 cells is given in Figure S5. (B) The 12 h incubation of 1 nM of each DN with BMDC. (C) L-shaped internalization efficiency in BMDCs. (D) S-shape internalization efficiency in BMDCs. Error bars are ±SD representing three triplicate data sets per object.

total of 11 DNs were designed, folded, purified, and characterized and then incubated with 3 different cell types.

Our structures were designed to represent a variety of geometric forms: round, square, solid, open, 3D, and quasi-2D (long rods). Unique to our approach and inherent to using the DNA origami as material platform is that structures folded with the same scaffold are identical in composition and mass. This allows us to control for these factors and, thus, truly analyze the

importance of structure and shape in NP uptake. Further, cell types differ vastly in their ability to uptake NPs in culture (for example, dendritic cells are professional endocytosing cells, whereas endothelial cells are often used as biological barriers and thus resist endocytosing circulating NPs). We chose to screen our DN library in diverse cell types relevant for understanding NP cellular uptake in in vivo conditions. By studying the effect of precision control in NP shape on cellular
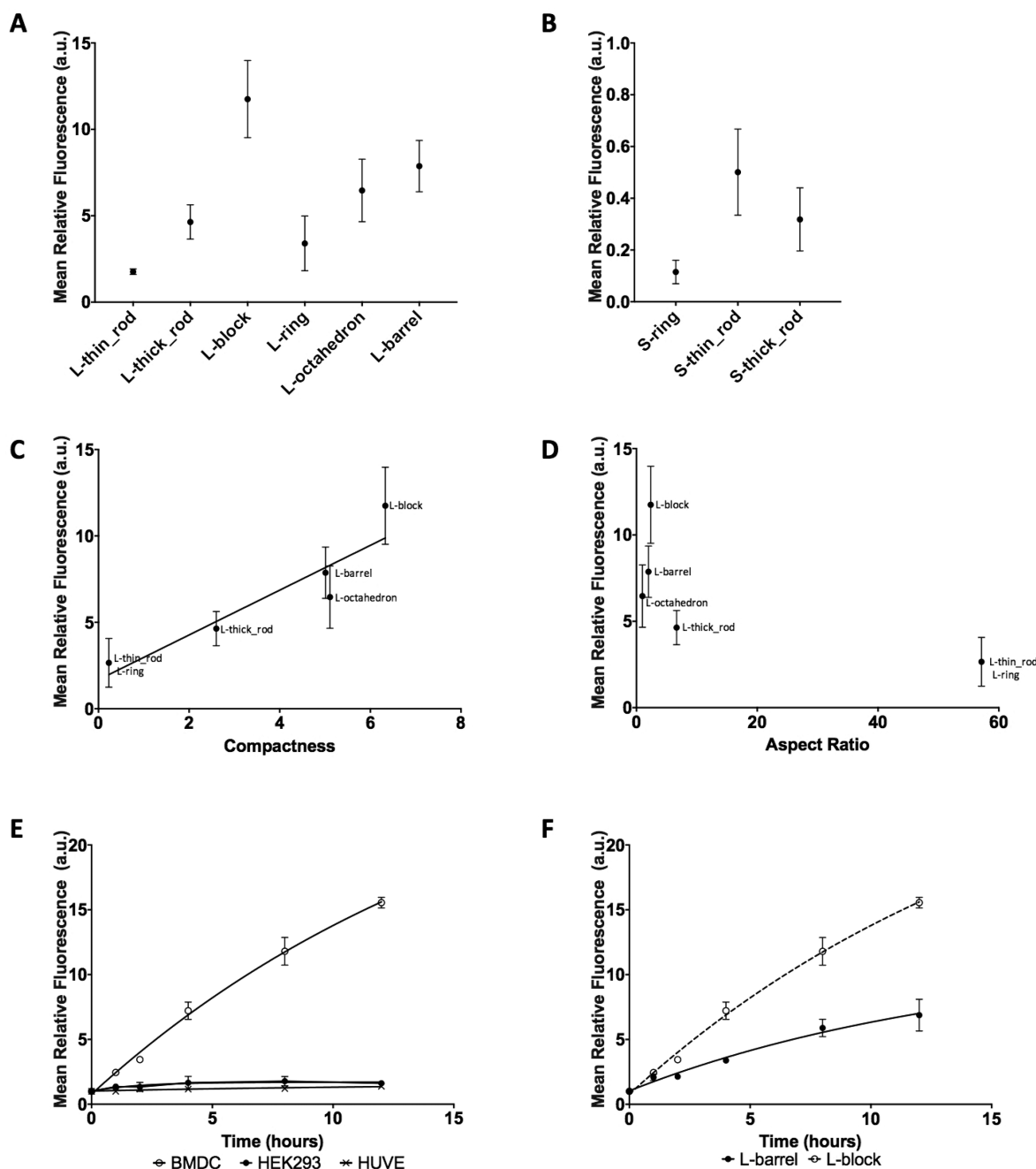
Figure 3. Quantitative analysis of DN uptake into mammalian cell types. (A) Cellular uptake of six L-shapes into BMDCs. Mean fluorescence is calculated relative to L-dsDNA. (B) Cellular uptake of three S-shapes into BMDCs. Mean fluorescence is calculated relative to S-dsDNA. (C) Compactness of shapes (see Table S3) vs cellular uptake of L-shapes relative to L-dsDNA. $R^2 = 0.84$. (D) Aspect ratio (see Table S3) vs cellular uptake of L-shapes relative to L-dsDNA. (E) Cellular uptake of L-barrel and L-block into BMDC over 12 h. (F) Cellular uptake of L-block across BMDC, HUVE, and HEK293 cell lines. In both panels E and F, uptake is shown relative to negative control, wherein no DN is added. For panels A–D, $n > 5$; for panels E and F, $n > 3$. Error bars are ±SD.

uptake using DNA nanotechnology, we afford new insights for future therapeutic NP design strategies.

Using the unprecedented control in nanoparticle uniformity inherent to the DNA-nanotechnology approach, we constructed a series of 11 DNA origami NPs of diverse shapes designed using caDNAno.[24] Structures were folded over a thermal ramp and purified using standard techniques (see the Supporting Information section 1 and Table S1). These structures, shown in Figure 1, ranged in their maximum dimension from 50 to 400 nm and were each tagged with three Cy5 fluorophores covalently conjugated to amine-modified

DNA staple strands present in the core of the origami structures. Our findings show these core-modified structures are preferentially uptaken by mammalian cells in comparison with DNs that are decorated with ssDNA or dsDNA handles (Figure S1).

One series of shapes (large, L-shapes of 5 MDa) were fabricated using a 7308-nucleotide-long scaffold (p7308) and consisted of 3 block-like shapes with varying aspect ratios (L-block, L-thick_rod, and L-thin_rod), 2 wireframe shapes (L-octahedron and L-ring), and a hollow cylinder shape (L-barrel). A second series of 3 analogous shapes (Small, or S-shapes of 2

MDa) was similarly constructed using a 3024-nucleotide-long scaffold (p3024) consisting of S-thick_rod, S-thin_rod, and S-ring. Corresponding cyclic double-stranded controls of mass 2 MDa (S-dsDNA) and 5 MDa (L-dsDNA) also were developed. The structural integrity of each shape was verified by agarose gel electrophoresis (AGE) and negative-stain transmission electron microscopy (TEM) (Figures S2 and S3). All constructed DN were free from aggregation and were predominantly found in the monomeric state. To ensure the stability of our DNs under low-salt conditions and to protect them from nuclease degradation, we coated the DN with oligolysine(K10)-PEG(5K) as recently reported.[23]

Once nanoparticles are administered into circulation, they can encounter various different types of cells, including endothelial, epithelial, and immune cells. Because therapeutic nanoparticles can be targeted to any of these cell types, we believe it is essential to screen the uptake of our particle library on these different cell types. All uptake studies were performed in a CO_2 incubator at 37 °C using human umbilical vein endothelial (HUVE) cells, bone-marrow-derived dendritic cells (BMDCs), and human embryonic kidney (HEK293) cells. Particle internalization was qualitatively assessed using confocal microscopy. Herein, 10 000 cells were seeded on microwell slides and allowed to adhere overnight. DNs were added and incubated with the cells for 12 h. A total of 30 min before imaging, Hoechst 33324 (final concentration 5 μg/mL) was added to each well and allowed to incubate. We confirmed that the addition of DNs at 1 nM concentration was sufficient for visualization and detection and that it was nontoxic to the cells (Figures 2A and S4). For all shapes, confocal imaging after overnight incubation was performed to qualitatively confirm uptake and viability of cells (Figures 2B and S5).

To quantitatively assess particle uptake, flow cytometry was performed, and the obtained fluorescent intensities were calibrated to the absolute fluorescence per shape. Cell-associated fluorescence signals measured by flow cytometry can result both from the extracellular adhesion of DNs to the cell membrane and from DN internalization. We therefore determined the external versus internal fraction of DN by comparing samples with or without digestion of the extracellular DN population with a high dose of DNaseI (20 units per well), which we confirmed digests DNs in culture medium (Figure S6). Our studies with BMDCs revealed that, for particles co-localized with cells, between 45−70% had been internalized (Figure 2C,D), and the remainder remained on the cell surface. Similar trends were found for the other cell lines (data not shown). Following this observation, all further analyses in this study only considered the internalized population of DNs.

To answer the question of whether or not particle shape affects uptake efficiency, we incubated our complete DN library with all three cell lines and measured uptake efficiency via flow cytometry after 12 h of incubation. Uptake of all shapes was measured using independent passages for HUVE and HEK293 cells and freshly matured BMDCs (Figures 3A,B and S6). Fluorescence was shape-specifically calibrated (Table S2), and overall uptake was normalized to the dsDNA control of corresponding mass (either L-dsDNA or S-dsDNA). BMDCs showed the most-pronounced variation dependent on shape, with internalization up to 15-fold greater for the compact L-block structure than for the dsDNA control. Between larger scale DNs with shapes of equal mass (p7308, L-shapes), shapes with greater compactness (which we operationally define here

as $ASA^{1.5}/EV$, where ASA is accessible surface area and EV is effective volume; see Table S3) were preferentially internalized after 12 h regardless of structure-type (hollow or solid); see Figure 3C. Interestingly, this trend prevailed across cell types, whereas multiple previous reports show differing preferences for particle shape of HUVE and HEK293 cells and BMDCs for anionic polymeric NPs.[13] Furthermore, a linear correlation between DN compactness and uptake efficiency was observed (R^2 = 0.84). DNs with smaller aspect ratios (between 1 and 3) were taken up most favorably by BMDCs (Figure 3D). For the smaller-mass DNs (p3024, S-shapes), the results indicate more cell-type and shape-related differences. BMDCs internalized all small DNs at a similar amount, although less rapidly than in the S-dsDNA control.

For BMDCs, we observed that at 12 h, L-block was present at twice the concentration inside the cell compared to L-barrel structures, indicating the preferential uptake of L-block ($p < 0.005$). These structures are highly similar in size and mass and differ most significantly in structure-type: the block is a solid structure, whereas the barrel is hollow. To test further whether hollowness is correlated with slower internalization, we compared the cellular uptake of the L-block to that of the L-octahedron. The L-octahedron again retains similar mass and size to the L-block but is wire-framed and hollow. Here again, the L-block was taken up significantly better ($p < 0.001$), whereas barrel and octahedron are taken up without significant difference ($p \gg 0.05$). Similarly, the L-block was most favorably taken up by both HEK293 and HUVE cell lines compared with other structures of similar mass. In these cell lines, L-block was taken up 3-fold better than a nonstructured particle of identical weight and roughly 2-fold better than the hollow barrel and octahedron structures (Figure S7).

L-sized blocks and barrels appeared to be among the most-preferred structures for endocytosis in all three cell lines, yet they are significantly different from each other. We postulated that their uptake kinetics may be cell-type-dependent. For both DNs, the uptake kinetics of particle internalization for each cell line over 12 h was evaluated (Figure 3E). We observed that the intracellular accumulation of both shapes for HUVE and HEK293 cells reach maximum fluorescence (i.e., amounts of internalized NPs) within 2 h (Figure S8). Longer incubation did not lead to further net accumulation of nanoparticles within the cells. For BMDCs, net accumulation of nanoparticles continued to occur throughout the 12 h of incubation and did not appear to plateau (Figure 3F). This correlate well with the notion that BMDCs are specialized endocytosing cells with likely a much-greater capacity for nanoparticle internalization. This trend was consistent for both shapes, suggesting that the rate of DN uptake is cell-type specific.

Recently, Wang et al. reported on the shape-biased uptake of DNs in lung cancer cells.[25] Rod-like and tetrahedral structures were evaluated in two different cell lines. Comparing large and small structures, they found that cells preferably internalized the larger ones, reasoning that enhanced surface interactions leads to higher uptake efficiency. However, their unstructured scaffold control displayed similar uptake levels, thereby suggesting the cancer cells minimally discriminate between true shape but rather respond to size variations through the engagement of multiple surface receptors. Our study complements their work and elaborates further on the true effect of shape variations. The L structures in our library indeed display superior uptake over S-particles. Additionally, within the seven L-DNs, a significant distribution of shape related uptake

efficiency was seen. The cellular uptake of NPs is mediated through size-specific mechanisms: caveolae-mediated uptake predominantly engages NPs up to 500 nm, whereas clathrin-coated pits commonly act to endocytose particles smaller than 200 nm. Our DN library lies squarely in this range and can therefore be used to elucidate the shape dependence of these pathways.

Our study demonstrates that for BMDCs and HUVE and HEK293 cells, a significant linear relationship between NP compactness and cell internalization efficiency exists. For DNs, compact shapes with a low aspect ratio in the size range of 50–80 nm are more efficiently internalized in all three cell types studied. The L-barrel leads in uptake efficiency, showcasing a 15-fold higher uptake level compared to a nonstructured DN of similar mass. Additionally, when comparing DNs of similar compactness, we observed solid DNs to be preferred over hollow or wire-frame structures ($p < 0.05$). For all high-aspect-ratio DNs (L-thin_rod and L-ring), moderate uptake was measured. Our high-aspect-ratio structures have very contrasting size dimensions, which could engage varying mechanisms for uptake partially causing their limited uptake efficiency. Further in-depth studies evaluating specific internalization pathways will be performed in future research. Uptake kinetics were largely cell-type-dependent, and saturation levels were reached quickly (<2 h) in HUVE and HEK293 cells but did not appear to plateau even after 12 h in BMDCs. These observations correlate well with the known biological function of endothelial cells as biological barriers and dendritic cells, which have highly active endocytosing profiles.

Utilizing the structural control inherent to the DNA origami technology, we here demonstrated that cells treat particles with the same mass but varying 3D appearance differently. This observation was consistent over multiple cell lines, suggesting that a preserved mechanism in cell-uptake is engaged. In particular, we highlight the importance of nanostructure compactness and aspect ratio. Shape also has demonstrated importance in the selective entry of pathogens into mammalian cells. Pathogens exhibit a remarkable diversity of evolutionarily conserved forms. These result, in part, from selective pressures deriving from the effect of shape on cellular uptake. Comprehensive of the contribution of shape to cellular uptake is often poor due to engineering challenges in mimicking pathogen shapes with accuracy. We believe DNs to be an ideal tool for furthering investigations along this theme.

Unsurprisingly, of the three cell types examined (endothelial, epithelial, and immune cells), immune cells (BMDCs), showed the highest rate of internalization and highest internalization efficiency. This correlates with the notion that BMDCs are specialized endocytosing cells. Our data set demonstrates that certain structural shapes are preferentially internalized by BMDCs. DNs are unique in their ability to self-assemble into precise nanoscale complexes. When modified with biologically active molecules, they can trigger cellular mechanisms including immune responses as reported in early studies.[26–28] Our presented insights into shape-dependent uptake afford new guidelines for NP design strategies for optimizing DNs for cellular uptake and further downstream immunological applications.

An important consideration for the interpretation of these DN uptake studies is that a large fraction of DNs associated with cells at a steady state remains on the cell surface and are not internalized. With the rapid expansion of the DNA origami technology to therapeutic applications, our presented insights

into the relation of shape and aspect ratio to cell-uptake provide a starting guide toward application oriented design principles of DN therapeutics.

Fabrication of DNs. A total of 11 DNA origami objects were designed using caDNAno and assembled using the previously published 3D DNA origami methods.[24] Construction plans for all objects and staple sequences are listed in section 1 of the Supporting Information. All synthetic DNA was purchased on a 100 nmole scale in 96-well plates from IDT. p7308 and p3024 scaffolds were produced in house using previously published protocols,[29] and purified from endotoxins before use.[30]

A total of four shapes (S-dsDNA, S-ring, S-thin_rod, and S-thick_rod) were assembled using a 3024-nucleotide ssDNA with a sequence based on the pBluescript phagemid vector (section 1 of the Supporting Information). The remaining shapes (L-dsDNA, L-ring, L-thin_rod, L-thick_rod, L-block, L-barrel, and L-octahedron) were built using a 7308 nucleotide ssDNA with a sequence based on the M13 genome (section 1 of the Supporting Information). To construct dsDNA controls of 2 and 5 MDa molecular weights (S-dsDNA and L-dsDNA), the p3024 and p7308 scaffolds were uniformly tiled with complimentary 42 mer oligonucleotides (section 1 and Supporting Table 1 in the Supporting Information)

Folding conditions used were 5 mM Tris, 1 mM EDTA at pH of 8.0, 50 nM scaffold strand, 100 nM staple strands, and $MgCl_2$ at a concentration that varied depending on the design to maximize design-specific yield: S-dsDNA, 8 mM; S-ring, 8 mM; S-thin_rod, 10 mM; S-thick_rod, 10 mM; L-dsDNA, 10 mM; L-ring, 8 mM; L-thin_rod, 8 mM; L-thick_rod, 12 mM; L-block, 14 mM; L-barrel, 10 mM; and L-octahedron, 18 mM. The solutions were subjected to a thermal annealing ramp on a Tetrad 2 Peltier thermal cycler (Bio-Rad) according to the following schedules. For S-dsDNA, the schedule was: denaturing (5 min) at 60 °C, annealing at 60–25 °C over 66 h at 1 °C steps; for S-ring: denaturing (5 min) at 60 °C, annealing at 60–25 °C over 66 h, at 1 °C steps; for S-thin_rod, denaturing (5 min) at 60 °C, annealing at 60–25 °C over 66 h at 1 °C steps; for S-thick_rod, denature (5 min) at 60 °C, annealing at 55–35 °C over 66 h at 1 °C steps; for L-dsDNA, denaturing (5 min) at 80 °C, annealing at 50–40 °C over 66 h at 1 °C steps; for L-ring, denaturing (5 min) at 80 °C, annealing at 65–25 °C over 66 h at 1 °C steps; for L-thin_rod, denaturing (5 min) at 80 °C, annealing at 65–25 °C over 66 h at 1 °C steps; for L-thick_rod, denaturing (5 min) at 80 °C, annealing at 55–49 °C over 66 h at 1 °C steps; for L-block, denaturing (5 min) at 80 °C, annealing at 55–40 °C over 66 h at 1 °C steps; for L-barrel, denaturing (5 min) at 65 °C, annealing at 50–40 °C over 66 h at 1 °C steps; and for L-octahedron, denaturing (5 min) at 80 °C, annealing at 65–25 °C over 66 h at 1 °C steps. All objects were purified using PEG precipitation (vide infra). The quality of folding was analyzed by agarose gel electrophoresis (Figure S2).

Fluorescent Labeling of DNs. For the fluorescence analysis of particle uptake, three staple strands for each DN were selected and modified with a 3′ amine. Cy5 fluorophores were covalently coupled through NHS ester coupling (http://www.lumiprobe.com/p/cy5-nhs-ester) In an Eppendorf tube (covered in foil to ensure darkness), a total of 15 μL of 1 mM oligo in double-distilled water (ddH$_2$O), equal to 15 nmol of oligo, 15 μL of 25 mM NHS-Cy5 in DMSO equal to 375 nmol of dye (25× excess), and 3.3 μL of 1 M NaHCO$_3$ buffer at pH 8.1 (sterile filtered) was combined for a total volume of 33.3

μL. The reaction proceeded for 3 h at room temperature in a dark room. Zeba size-exclusion and desalting columns (7K MWCO; Thermo Scientific, Waltham, MA) were used to remove unreacted dye through centrifugation at 1000*g* for 2 min. The columns were washed with 400 μL of ddH₂O three times before use according to manufacturer's protocol.

PEG Precipitation for DN Purification. To the folded-DN stock solution, we added *x*% 8000 PEG, 0.25 M NaCl and 1× folding buffer (see the Fabrication of DNs section) in a 1:1 ratio. The concentration of PEG (*x*%) necessary was optimized for each shape (L-dsDNA: 7.5%; L-block: 5%; L-thin_rod: 5%; L-thick_rod: 5%; L-ring: 5%; L-octahedron: 5%; L-barrel: 5%; S-dsDNA: 10%; S-ring: 10%; S-thick_rod: 10%; and S-thin_rod: 10%). The mixed solutions were placed at room temperature for 30 min followed by a spin at 16000*g* for 40 min at 25 °C. The supernatant was removed from the pellet and set aside for AGE analysis. The pellet was resuspended in appropriate folding buffer for each shape and allowed to incubate for 30 min at room temperature to allow the structures to unpack. Purification quality was verified by AGE analysis.

Oligolysine-PEG5K Coating of DNs. A total of 10 μL of 20 nM origami structure was mixed 1:1 (v/v) with oligolysine-PEG (K10-PEG5K) to achieve 10 nM of the final DNA shape concentration. A concentration in which the desired 1:1 N-to-P ratio (ratio of nitrogen in amines:phosphates in DNA) would be achieved was calculated per shape23 (L-dsDNA: 29.7 μM; L-block: 27.3 μM; L-thin_rod: 29.7 μM; L-thick_rod: 29.6 μM; L-ring: 29.7 μM; L-octahedron: 27.2 μM; L-barrel: 41.4 μM; S-dsDNA: 12.6 μM; S-ring: 12.6 μM; S-thick_rod: 12.1 μM; and S-thin_rod: 12.6 μM). The samples were incubated at room temperature for 30 min. K10-PEG5K was purchased from Alamanda polymers, and their polydispersity index from gel-permeation chromatography is between 1.00 and 1.20.

TEM Studies. The structural integrity of all shapes was verified using negative-stain transmission electron microscopy. The TEM sample was prepared by dropping 3.5 μL of a 1 nM sample solution on a carbon-coated grid (400 mesh, Ted Pella). Before depositing the sample, the grids were negatively glow-discharged for 45 s. After 2 min, the sample was wicked from the grid by touching its edge with a piece of filter paper. Then the grid was touched with a drop of 2% uranyl formate solution, and excess solution was wicked away with a filter paper. TEM studies were conducted using a JEOL JEM-1400 transmission electron microscope, operated at 80 kV on bright-field mode.

Cellular-Uptake Assay. All uptake studies were performed using HUVE cells, BMDCs, and HEK293 cells. HUVE cells were maintained in EBM-2 media supplemented with Single-Quots growth factors and 2% fetal bovine serum (FBS; Lonza, Wakersville), HEK293 in high-glucose Dulbecco modified Eagle medium (Gibco, Gaithersburg) and 10% FBS with penicillin–streptococcus. BMDCs were derived using established methods.[31] Briefly, bone marrow cells were isolated from female C57Bl/6J mice (Jackson Laboratories) and cultured in RPMI (Lonza) supplemented with 10% heat-inactivated FBS (Sigma-Aldrich), 1% penicillin–streptomycin, 50 μM *β*-mercaptoethanol (Sigma-Aldrich), and 20 ng/mL−1 granulocyte–macrophage colony-stimulating factor (Peprotech). Non-adherent dendritic cells between days 7 and 10 were harvested and used for experiments.

For uptake studies, cells were seeded at a density of 100 000 cells per well into tissue-culture-treated 24-well plates (BD Life Sciences) and allowed to adhere overnight. For sample incubation, samples were prepared by diluting the purified

origami shapes to 10 nM concentration in folding buffer [5 mM Tris pH 8.5, *x* mM MgCl2 (*x* being specific to shape), and 1 mM EDTA] and then diluted to a final concentration of 1 nM after addition to the seeded cells (50 μL). Cells were then incubated at a final sample concentration of 1 nM at 37 °C overnight or for the described amount of times (for kinetic experiments). All samples were set up in triplicate, and the experiments were repeated on three different days.

Flow Cytometry. For flow-cytometry experiments, cells incubated with DNs were scraped and transferred to a 96-well plate. The samples were split over 2 plates (200 μL per plate), and 1 plate was incubated with 20 U DNaseI (NEB, Ipswich, MA) for 1 h at 37 °C. The fluorescently labeled samples were analyzed directly on a BD LSRfortessa SORP flow cytometer equipped with an optional high-throughput sampler sampler (BD Biosciences, San Jose, CA) using the following configuration: Cy5 excitation of 640 nm/40 mW and emission filter band-pass of 670 nm/30 mW. Data were analyzed using FlowJo (Tree Star, Ashland, OR), Prism (GraphPad, La Jolla, CA), and Excel (Microsoft, Redmond, VA) software.

Confocal Microscopy. For confocal microscopy experiments, 10 000 cells were seeded on tissue culture-treated 15-well ibidi slides (cat. no. 81506) and allowed to adhere overnight. DNs were added in a final concentration of 1 nM in 50 μL per well and incubated overnight. A total of 30 min before imaging, 1 μL of Hoechst 33324 (final concentration of 5 μg/mL) was added to each well and allowed to incubate. Cells were removed from the incubator and imaged on a Leica SP5 X MP inverted laser-scanning confocal microscope using a 63× water objective. Excitation for Cy5 was 640 nm and, for Hoechst 33324, was 350 nm; Z-stacks consisted of ~10 images per stack, spaced by 0.2 μm.

Normalization of Fluorescence Intensity. To enable a comparison of data among DNs, fluorescence intensity values within each of the 12 data sets were normalized before calculating their mean across the 12 sets. Normalization was performed by measuring the final DN concentration by Nanodrop (Nanodrop 2000, Thermo Scientific) and the fluorescence intensity of 20 μL in triplicate on a black 384-well plate on a BioTek NEO fluorescent plate reader with excitation at 645 nm (Cy5) (Table S2).

Each structure theoretically contains three Cy5-labeled oligonucleotides. To confirm the correct labeling, triplicates of Cy5 emission was measured of both the free Cy5-oligo and the Cy5-labeled DN. A calibration curve to relate Cy5 concentration to the intensity of the plate reader was prepared using 11 data points in concentration range of 10−200 nM, relevant for the DNA-shape origami structures. Measured intensities were correlated to the calibration curve and compared to the concentration measured by nanodrop concentration. To correct for non-incorporated excess of Cy5-labeled oligo, agarose-gel electrophoresis was performed for all shapes, and the intensity of both the origami and the free oligo was summed. The percentage of DN was calculated and used to correct the fluorescence data.

DNaseI Treatment. After sample incubation, cells were incubated with 20 U DNase I (NEB) for 60 min at 37 °C to allow for the digestion of non-internalized DNs. These conditions were optimized and shown to digest the oligolysine-PEG coated DNs (Figure S6).

Kinetic Uptake Experiments. Cells were seeded at 100 000 counts per well as before. Relevant DNs were added to a final concentration of 1 nM and incubated with cells for

periods of 0, 1, 2, 4, 8, and 12 h. After the prescribed incubation time, samples were prepared for flow cytometry as previously described.

ASSOCIATED CONTENT

Ⓢ Supporting Information

The Supporting Information is available free of charge on the ACS Publications website at DOI: 10.1021/acs.nano-lett.8b00660.

Additional details on materials and methods. Figures showing the handle–anti-handle design, AGE and TEM analysis of nanostructures, toxicity studies on HUVE cells, qualitative shape oversations, DNAseI digestion of DNA origami, flow cytometry, and a kinetic study of L-block and L-barrels for HEK293 and HUVE cells. Tables showing a staple listing of nine DNA nanostructures, fluorescence calibration, and characteristics for each DNA nanostructure. (PDF)

AUTHOR INFORMATION

Corresponding Authors
*E-mail: jhryu@kist.re.kr. Phone: +1-(617)-632-5184.
*E-mail: William_Shih@dfci.harvard.edu. Phone: +1-(617)-632-5143.

ORCID Ⓘ
Chenxiang Lin: 0000-0001-7041-1946
Donald E. Ingber: 0000-0002-4319-6520
William M. Shih: 0000-0002-1395-9267

Present Addresses
#Institute of Materials, School of Engineering, École Polytechnique Fédérale de Lausanne, CH-1015 Lausanne, Switzerland.
∇Nanobiology Institute, Yale University, West Haven, CT 06516, United States.

Author Contributions
∞M.M.C.B, F.M.A., and N.P. contributed equally to this work. F.L., C.L., D.E.I., and W.M.S. designed the original study. M.M.C.B., F.M.A., N.P., and J.H.R. produced the DNA library. M.M.C.B. and F.M.A. performed all of the cell studies. G.C. assisted in flow cytometry. M.M.C.B., F.M.A., N.P., J.H.R., and W.M.S. wrote the manuscript.

Notes
The authors declare no competing financial interest.

REFERENCES

(1) Allen, T.; Cullis, P. R. *Science* **2004**, *303*, 1818−1822.
(2) Blanco, E.; Shen, H.; Ferrari, M. *Nat. Biotechnol.* **2015**, *33*, 941−951.
(3) Gratton, S. E.; Ropp, P. A.; Pohlhaus, P. D.; Luft, J. C.; Madden, V. J.; Napier, M. E.; DeSimone, J. M. *Proc. Natl. Acad. Sci. U. S. A.* **2008**, *105*, 11613−11618.
(4) Young, K. D. *Microbiol. Mol. Biol. Rev.* **2006**, *70*, 660−703.
(5) Champion, J. A.; Mitragotri, S. *Proc. Natl. Acad. Sci. U. S. A.* **2006**, *103*, 4930−4934.
(6) Wang, J.; Byrne, J. D.; Napier, M. E.; DeSimone, J. M. *Small* **2011**, *7*, 1919−1931.
(7) Tao, L.; Hu, W.; Liu, Y.; Huang, G.; Sumer, B. D.; Gao. *Exp. Biol. Med.* **2011**, *236*, 20−29.
(8) Rejman, J.; Oberle, V.; Zuhorn, I. S.; Hoekstra, D. *Biochem. J.* **2004**, *377*, 159−169.
(9) Desai, M. P.; Labhasetwar, V.; Walter, E.; Levy, R. J.; Amidon, G. L. *Pharm. Res.* **1997**, *14*, 1568−1573.
(10) Chithrani, B. D.; Ghazani, A. A.; Chan, W. C. W. *Nano Lett.* **2006**, *6*, 662−668.
(11) Florez, L.; Herrmann, C.; Cramer, J. M.; Hauser, C. P.; Koynov, K.; Landfester, K.; Crespy, D.; Mailänder, V. *Small* **2012**, *8*, 2222−2230.
(12) Chithrani, B. D.; Chan, W. C. W. *Nano Lett.* **2007**, *7*, 1542−1550.
(13) Schaeublin, N. M.; et al. *Langmuir* **2012**, *28*, 3248−3258.
(14) Agarwal, R.; Singh, V.; Jurney, P.; Shi, L.; Sreenivasan, S. V.; Roy, K. *Proc. Natl. Acad. Sci. U. S. A.* **2013**, *110*, 17247−17252.
(15) Geng, Y.; Dalhaimer, P.; Cai, S.; Tsai, R.; Tewari, M.; Minko, T.; Discher, D. E. *Nat. Nanotechnol.* **2007**, *2*, 249−255.
(16) Seeman, N. C. *J. Theor. Biol.* **1982**, *99*, 237−247.
(17) Seeman, N. C. *Annu. Rev. Biochem.* **2010**, *79*, 65−87.
(18) Rothemund, P. W. K. *Nature* **2006**, *440*, 297−302.
(19) Douglas, S. M.; Dietz, H.; Liedl, T.; Högberg, B.; Graf, F.; Shih, W. M. *Nature* **2009**, *459*, 414−418.
(20) Linko, V.; Ora, A.; Kostiainen, M. A. *Trends Biotechnol.* **2015**, *33*, 586−594.
(21) Perrault, S. D.; Shih, W. M. *ACS Nano* **2014**, *8*, 5132−5140.
(22) Agarwal, N. P.; Matthies, M.; Gur, F. N.; Osada, K.; Schmidt, T. L. *Angew. Chem., Int. Ed.* **2017**, *56*, 5460−5464.
(23) Ponnuswamy, N.; Bastings, M. M. C.; Nathwani, B.; Ryu, J. H.; Chou, L. Y. T.; Vinther, M.; Li, W. A.; Anastassacos, F. M.; Mooney, D. J.; Shih, W. M. *Nat. Commun.* **2017**, *8*, 15654.
(24) Douglas, S. M.; Marblestone, A. H.; Teerapittayanon, S.; Vazquez, A.; Church, G. M.; Shih, W. M. *Nucleic Acids Res.* **2009**, *37*, 5001−5006.
(25) Wang, P.; Rahman, M. A.; Zhao, Z.; Weiss, K.; Zhang, C.; Chen, Z.; Hurwitz, S. J.; Chen, Z. G.; Shin, D. M.; Ke, Y. *J. Am. Chem. Soc.* **2018**, *140*, 2478−2484.
(26) Schuller, V. J.; Heidegger, S.; Sandholzer, N.; Nickels, P. C.; Suhartha, N. A.; Endres, S.; Bourquin, C.; Liedl, T. *ACS Nano* **2011**, *5*, 9696−9702.
(27) Li, J.; Pei, H.; Zhu, B.; Liang, L.; Wei, M.; He, Y.; Chen, N.; Li, D.; Huang, Q.; Fan, C. *ACS Nano* **2011**, *5*, 8783−8789.
(28) Liu, X.; Xu, Y.; Yu, T.; Clifford, C.; Liu, Y.; Yan, H.; Chang, Y. *Nano Lett.* **2012**, *12*, 4254−4259.
(29) Douglas, S. M.; Chou, J. J.; Shih, W. M. *Proc. Natl. Acad. Sci. U. S. A.* **2007**, *104*, 6644−6648.
(30) Hahn, J.; Wickham, S. F. J.; Shih, W. M.; Perrault, S. D. *ACS Nano* **2014**, *8*, 8765−8775.
(31) Bhattacharya, P.; Gopisetty, A.; Ganesh, B. B.; Sheng, J. R.; Prabhakar, B. S. *J. Leukocyte Biol.* **2011**, *89*, 235−249.